Influence of Geological and Geomorphological Factors on Vertical Co-Seismic Deformation Induced by the Mw 7.2 Al Haouz Earthquake (Morocco, 2023)

Adnane Habib [1], Ayoub El Adnani [2], Ilyasse Berrada [3], Amine Naji [4], Ahmed Fadili [5], Youness Ahmed Laaziz [6], Taha Youness Arrad [7], Abdelouahed Lagnaoui [8,9]

[1] ESIM, Polydisciplinary Faculty of Sidi Bennour, Chouaïb Doukkali University, El Jadida, Morocco
[2] Laboratoire Géosciences Marines et Sciences des sols (LGMSS-URAC45), Faculty of Sciences, Chouaïb Doukkali University, El Jadida, Morocco
[3] Science and Technology Research Laboratory (LRST), Higher School of Education and Training Agadir (ESEFA), Ibnou Zohr University, Agadir, Morocco
[4] Geosciences Laboratory - LPG, UFR Sciences et Techniques, Maine University, Le Mans, France
[5] Polydisciplinary Faculty of Ouarzazate, Ibnou Zohr University, Ouarzazate, Morocco
[6] Ecole Normale Supérieure (ENS), Mohammed V University in Rabat, Rabat, Morocco
[7] Laboratory of Geodynamic and Geomatic, Faculty of Sciences, Chouaïb Doukkali University, El Jadida, Morocco
[8] LIRSEF, Higher School of Education and Training Berrechid (ESEFB), Hassan First University, Berrechid, Morocco
[9] LSOGBR, Institute of Geology and Petroleum Technologies, Kazan (Volga Region) Federal University, Kazan, Russia

Keywords: Co-seismic deformation, DInSAR, DEM, Landform, Terrain analysis, Al Haouz earthquake.

Abstract

This study analyzes the influence of structural, lithological, and geomorphological factors on vertical co-seismic deformation caused by the Mw 7.2 Al Haouz earthquake of 8 September 2023 in Morocco. Vertical deformation, derived from Differential InSAR analysis of Sentinel-1A imagery, was compared with lithological units, fault structures, and terrain attributes extracted from the FABDEM digital elevation model, including slope, aspect, and geomorphon-based landform classes. Results show that deformation was strongly controlled by geology. Cambrian shaly formations, known for their plasticity and instability, exhibited the highest vertical displacements. Proximity to faults also enhanced deformation, with a 1000 m buffer around mapped faults yielding mean uplift of 5.3 cm (SD = 5.4 cm) and deformation gradients averaging 1.02% (SD = 1.8%). Topography played a significant role. Flat areas (<5°) generally subsided (–2.6 cm), while steeper slopes showed uplift, peaking at 5.4 cm near 45°. Slope orientation influenced deformation distribution: northeast-, east-, southeast-, and south-facing slopes recorded uplift (1.5–3.2 cm), whereas north- and northwest-facing slopes and flats showed subsidence (–0.9 to –1.6 cm). Landform analysis revealed systematic variations. Subsidence dominated flat, shoulder, and footslope forms, while uplift prevailed in pits, hollows, spurs, ridges, and peaks. Spurs in particular displayed strong deformation (mean uplift: 2.9 cm, SD = 10.6 cm), with ~11% of deformation boundaries coinciding with spur boundaries, suggesting they act as structural controls on rupture propagation. Overall, the findings demonstrate that lithology, faulting, and terrain morphology jointly modulate co-seismic deformation. Integrating DInSAR with terrain analysis provides valuable insights into earthquake surface processes and spatial hazard assessment.

1. Introduction

The study of earthquake-induced ground deformation is fundamental to understanding crustal processes, seismic hazards, and fault kinematics. Ground displacements associated with large earthquakes reflect the partitioning of seismic energy within the lithosphere and provide key information on fault geometry and slip distribution. With the advent of Interferometric Synthetic Aperture Radar (InSAR), researchers can now measure ground deformation with centimeter-level accuracy associated to natural causes as well as human-induced causes across large spatial extents (Ibrahim et al., 2025; Luo et al., 2024; Habib et al., 2017). InSAR-derived deformation fields have become indispensable for rapidly characterizing earthquake impacts and constraining geophysical models of fault behavior (Habib et al., in press, Habib et al., 2025, Hamdi et al., 2023; Li et al., 2021).

Although InSAR has been widely used to detect and quantify earthquake deformation globally, most previous works have largely emphasized fault mechanics, and relatively few studies have systematically linked InSAR-derived deformation patterns with the underlying geological and geomorphological features and how they can modulate the spatial expression of deformation (Torre et al., 2024; Abbas et al., 2022; Ramza et al., 2022; Rachael et al., 2014).

Linking the co-seismic deformation with geological and geomorphological characteristics provides deeper insights into how seismic energy is accommodated at the surface. The influence of these features on the spatial variability of co-seismic deformation is especially relevant in tectonically complex and topographically rugged regions. Such integration is essential for refining seismic hazard assessments and improving understanding of the relationship between active tectonics and surface processes, particularly in intraplate mountain belts like the Moroccan Atlas.

This study aims to evaluate the influence of structural, lithological, and geomorphological characteristics on vertical co-seismic deformation associated with the Al Haouz earthquake. By combining InSAR-derived co-seismic deformation with topographic and geological features, we investigate the primary controls governing deformation patterns in complex intraplate terrains. The results highlight the utility of integrating remote sensing and geospatial analysis to better understand earthquake processes and improve seismic hazard assessment in mountainous regions.

2. Study Site

2.1 The 2023 Al Haouz Earthquake

The Mw 7.2 Al Haouz earthquake occurred on September 8, 2023, at 22:11:01 GMT, representing the strongest seismic event ever recorded in Morocco by national seismic stations. The epicenter was located in the High Atlas Mountains (30.99° N, 8.41° W) within the rural commune of Ighil, with a focal depth of 10.7 km. Approximately 20 minutes after the main shock, a notable aftershock of Mw 4.9 was recorded. The event caused widespread devastation, leading to nearly 3,000 fatalities, extensive structural collapse, and severe damage.

2.2 Topographic Context

The Al Haouz region is characterized by a marked topographic contrast between the Haouz plain and the surrounding High Atlas Mountains. The plain lies at relatively low elevations, generally between 300 and 1,000 m, forming a broad alluvial depression at the northern foot of the chain (Algouti et al., 2016; Babault et al., 2012). In contrast, elevations rise sharply toward the High Atlas summits, culminating at Jbel Toubkal (4,165–4,167 m), the highest peak in Morocco and North Africa (Hughes et al., 2011; Ettachfini et al., 2018).

This altitudinal gradient results in a wide range of landforms, from piedmont glacis and fluvial terraces in the lowlands to deeply incised valleys and narrow ridges in the mountain domain. The drainage network is highly entrenched, with narrow gorges upstream and depositional plains downstream (Babault et al., 2012). At higher elevations, traces of Quaternary glaciations remain preserved, including cirques, moraines, and U-shaped valleys (Hughes et al., 2011).

Such a diverse topographic framework, combining flat depositional surfaces with steep erosional slopes, exerts a major influence on the spatial variability of ground deformation. It therefore provides an essential geomorphological context for interpreting the heterogeneous surface responses associated with the 2023 Al Haouz earthquake.

2.3 Geological Context

The Al Haouz epicentral zone lies in the western High Atlas (Figure 1), where a Variscan-deformed Paleozoic basement is unconformably overlain by Mesozoic–Cenozoic cover later inverted during the Alpine orogeny (Frizon de Lamotte et al., 2008). Early Cambrian successions comprise clastic–carbonate series with abundant volcanics and intrusions recording magma-rich rifting of NW Gondwana; Middle Cambrian–Ordovician siliciclastics mark rift abortion, with localized transgressive Late Visean strata to the east (Ettachfini et al., 2018). The cover includes thin Upper Jurassic evaporites and, after erosional gaps, Neocomian–Barremian red beds followed by Aptian–Middle Eocene shallow-marine deposits and syntectonic Late Miocene–Pliocene molasse (Froitzheim, 1984; Ettachfini et al., 2018).

Basement structuring reflects inversion of Cambrian rift faults during the Variscan, producing west-verging folds bounded by major E–W and NNE faults (Adassil–Medinet, Assif Anougal, Assif El Mal) (Ettachfini et al., 2018). In the Azegour area, two Paleozoic blocks—the Azegour Block (with preserved Cretaceous–Tertiary cover) and the more exhumed Erdouz Block—are separated by the Adassil–Medinet Fault; Early Cambrian volcanic-rich sequences typify the Erdouz Block and the High Atlas style (Ettachfini et al., 2018). Upper Jurassic strata (Timsilline Formation) thin eastward and are overlain discordantly by Lower Cretaceous red sandstones (Duffaud et al., 1966; Ettachfini et al., 2018).

Cenozoic to Quaternary evolution records Alpine shortening, uplift, and surface processes: Paleocene–Eocene units occur locally along fault zones; Neogene fluvial molasse thickens toward the Atlas; Quaternary deposits range from river terraces to periglacial and glacial features in the Toubkal massif, with moraines dated by cosmogenic isotopes and drainage reorganization from longitudinal to transverse systems (Algouti et al., 2016; Babault et al., 2012; Hughes et al., 2011).

This litho-structural complexity highlights the interplay of rifting, compressional tectonics, and surface processes that have shaped the High Atlas and directly influenced the seismic behavior of the Al Haouz region.

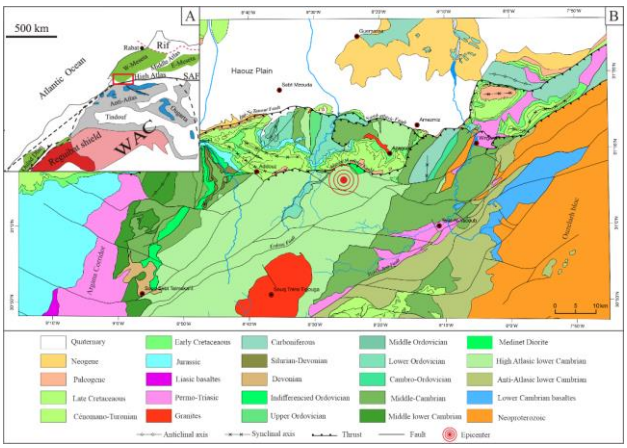

Figure 1. (A) Map showing the position of the Western High Atlas to the north of the Anti-Atlas domain (Adapted from Michard et al., 2008). (B) Structural scheme of the northern flank of the Western High Atlas and the northern sub-atlasic zone (Fekkak et al., 2018b).

3. Materials and Methods

To estimate and measure the surface deformation caused by the seismic activity, we used Sentinel-1A Interferometric Wide Swath (IWS) Single Look Complex (SLC) products. The dataset consisted of a pair of ascending orbit images (3 September 2023 and 15 September 2023) and a pair of descending orbit images (30 August 2023 and 11 September 2023). These SAR datasets were processed to generate differential interferograms and corresponding line-of-sight (LOS) deformation maps, from which vertical deformation was derived. The full InSAR processing workflow and preliminary results are described in (Habib et al., in press).

Elevation data were derived from the Forest And Buildings removed Copernicus DEM (FABDEM), which provides a clean and consistent bare-earth representation by minimizing biases from buildings and vegetation (Hawker et al., 2023). FABDEM has been shown to outperform SRTM in both statistical and visual assessments (El Mhamdi et al., 2024), offering improved capability for detailed analysis of topographic variations that may influence earthquake-induced deformation. Therefore, the FABDEM was used to extract terrain parameters such as slope

and aspect. Additionally, a geomorphon classification was applied to identify distinct landform types, such as ridges, valleys, and plains, providing a categorical representation of the geomorphological setting.

To investigate the influence of structural controls, zonal statistics were computed within buffers of varying distances around mapped fault lines. This procedure enabled the quantification of deformation patterns relative to tectonic structures, highlighting spatial variability in deformation intensity. The same procedure was applied to terrain attributes and geomorphon-derived landform classes, enabling the assessment of their relationship with vertical co-seismic deformation (Figure 2).

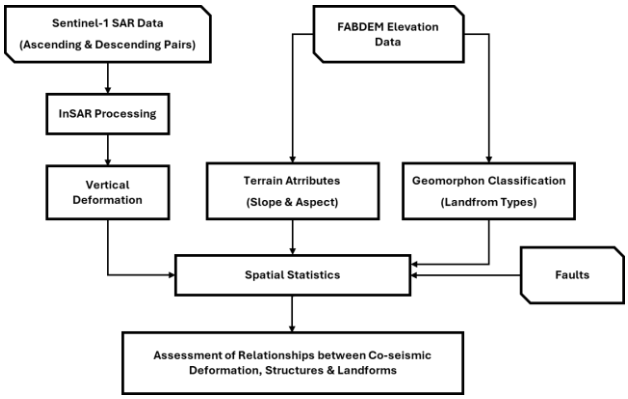

Figure 2. Flowchart of the methodology.

4. Results and Discussion

4.1 Vertical Deformation Patterns

The epicentral region recorded the strongest vertical co-seismic deformation, with uplift values reaching up to 36 cm, marking the zone of maximum crustal displacement and energy release (Figure 3). This pronounced uplift indicates intense tectonic activity and localized crustal shortening associated with the earthquake. Conversely, subsidence of about 5 cm was detected along the southwestern and northwestern flanks of the deformation corridor bounded by the Tizi N'Test and North Atlasic Faults. The sharp transition between uplift and subsidence aligns closely with the trace of the Tizi N'Test Fault, pointing to its direct involvement in rupture propagation. A similar pattern observed along the North Atlasic Fault further supports its active contribution to the seismic deformation. Taken together, these observations suggest that the vertical displacements were predominantly governed by an ENE-dipping thrust fault mechanism, which exerted a first-order control on the geometry and distribution of the observed ground deformation.

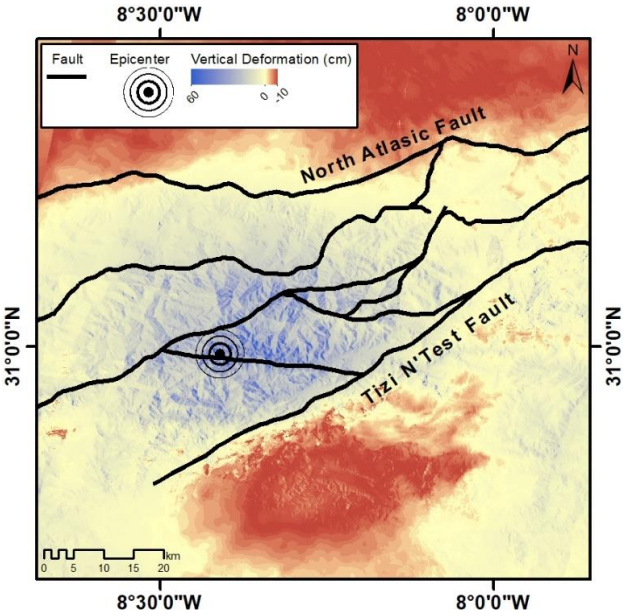

Figure 3. Vertical deformation map of the Al Haouz earthquake (Habib et al., in press).

4.2 Lithological and Faults Influence

Overlaying lithological units on the vertical deformation map revealed that zones exhibiting the highest deformation values correspond to Cambrian formations characterized by predominantly shaly, soap-like deposits. These formations, prone to plastic deformation, are also known for their susceptibility to landslides and terrain instability, especially under intense rainfall conditions. A zonal statistical analysis of vertical deformation and deformation gradient within a 1000-meter buffer around mapped faults showed a mean vertical deformation of 5.3 cm (standard deviation (SD) = 5.4 cm), indicating substantial variability and high displacements that occurred near the fault structures. The corresponding deformation gradient had a mean of 1.02% (SD = 1.8%), suggesting moderately steep spatial deformation patterns possibly associated with localized ruptures, fault scarps, or terrain-driven amplification effects.

4.3 Slope and Aspect Influence

Further analysis focused on terrain slope showed a clear association between slope angle and deformation behavior. Flat areas (slope < 5°) experienced subsidence, with a mean deformation of –2.6 cm (Figure 4). As slope angle increased, mean deformation shifted to positive values, peaking at approximately 5.4 cm for slopes around 45°, likely reflecting the capacity of steeper, more rigid slopes to accumulate and release seismic energy.

The relationship between slope steepness and vertical deformation reveals important insights into the mechanical response of terrain under seismic stress. Subsidence observed in the flattest zones (0-5°) may be attributed to sediment compaction or lack of structural support during ground shaking. As slopes increase, the terrain becomes more rigid and capable of storing and releasing energy, leading to more pronounced uplift. The peak in average uplift at slope classes between 25° and 45° suggests that these inclinations might coincide with optimal geometrical conditions for amplification of seismic energy or enhanced stress concentration. However, the observed reduction in uplift in the steepest slopes (above 60°) could be

due to gravitational relaxation, localized mass movements, or fewer representative pixels in the dataset.

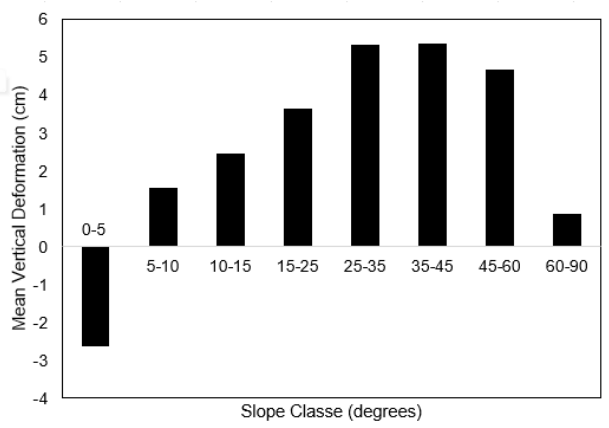

Figure 4. Mean vertical deformation distribution by slope classes.

Aspect-based analysis revealed distinct patterns in vertical deformation depending on slope orientation, with the highest uplift values observed on slopes facing northeast (1.5 cm), east (3.2 cm), southeast (3.1 cm), and south (1.7 cm), while north- and northwest-facing slopes, as well as flat terrains, generally experienced subsidence ranging from –0.9 to –1.6 cm (Figure 5). The highest values of uplift in north-, east-, southeast-, and south-facing slopes could be linked to the orientation of seismic wave propagation or fault movement. These slopes may have amplified vertical displacement due to their orientation relative to the seismic stress. On the contrary, subsidence in north-, northwest-facing and flat areas may result from reduced dynamic amplification or sediment compaction processes.

Figure 5. Mean vertical deformation distribution by slope aspects.

4.4 Landform Effects

Landform determination using the geomorphon-based landform classifications identified ten distinct landform types. Statistical analysis showed that subsidence was mainly associated with flat, shoulder, and footslope landforms (mean deformation: –3.5 cm, –2.6 cm, and –2.6 cm, respectively). These results may reflect in the case of shoulders local compression, compaction, or downslope material transfer during ground shaking. In contrast, uplift movement was dominant in pits (mean: 5.2 cm; SD: 4.3 cm), hollows, spurs, slopes, valleys, peaks, and ridges (Figure 6). Deformation gradients for these landforms reflected similar trends, with the highest values (~1.7%) again associated with pits. Beside the high values shown in the case of pits, which can reflect areas of localized stress or rapid change, spurs, in particular, emerged as significant zones of deformation, with a mean uplift of 2.9 cm and a notably high variability (SD = 10.6 cm), suggesting their potential role in rupture propagation or localized stress concentration. An intersection analysis between vertical deformation interval boundaries and landform boundaries further highlighted the influence of terrain morphology on vertical deformation distribution. Approximately 11% of deformation class boundaries were found to align with spur boundaries, reinforcing the hypothesis that spurs may act as structural boundaries guiding the spatial distribution of ground displacement during seismic events. Ridges and peaks also showed moderate uplift (~1.8 cm), reflecting their topographic resilience and potential structural connection to uplift zones.

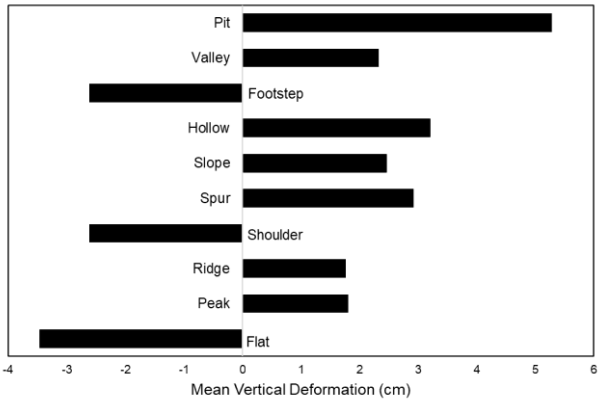

Figure 6. Mean vertical deformation distribution by landform types.

5. Conclusion

This study examines the influence of structural, lithological, and geomorphological characteristics on vertical co-seismic ground deformation associated with the Mw 7.2 Al Haouz earthquake, which occurred on 8 September 2023 in the Al Haouz region of Morocco. The vertical deformation, previously estimated using Differential Interferometric Synthetic Aperture Radar (DInSAR) analysis of Sentinel-1A satellite imagery, served as the basis for assessing the relationships between observed deformation and underlying geological and geomorphological features. The geological analysis relied on existing data, including fault line mapping and lithological units. For terrain-based parameters, the FABDEM (Forest And Buildings removed Copernicus Digital Elevation Model) was employed to extract slope, aspect, and geomorphon-based landform classification. Statistical analyses were then conducted to evaluate the spatial correlation between vertical deformation and these terrain attributes.

Overall, these results underscore the importance of integrating geological and geomorphological features when analyzing earthquake-induced surface deformation. The observed correlations between vertical deformation patterns, lithology, faults and terrain morphology; including slope, aspect, and landform type, demonstrate that faults, lithology, and geomorphology are significant contributors to the heterogeneity

of seismic surface responses. These findings highlight the utility of combining DInSAR techniques with DEM-derived terrain analyses for advancing the understanding of earthquake surface effects and spatial hazard modelling.

Acknowledgments

The authors acknowledge the use of AI generative tools in the preparation of the manuscript, with all content carefully assessed for clarity and reliability.

References

Algouti, A., Algouti, A.B., Hadach, F., 2016. Mise en évidence d'une phase tectonique au Santonien du versant Nord du Haut Atlas Occidental, Maroc. Eur. Sci. J., 12(3), 1857–7431.

Babault, J., Van Den Driessche, J., Teixell, A., 2012. Longitudinal to transverse drainage network evolution in the High Atlas (Morocco): The role of tectonics. Tectonics, 31, TC4020, doi:10.1029/2011TC003015.

Bullock, R.J., De Paola, N., Holdsworth, R.E., Trabucho-Alexandre, J., 2014. Lithological controls on the deformation mechanisms operating within carbonate-hosted faults during the seismic cycle. J. Struct. Geol., 58, 22–42. https://doi.org/10.1016/j.jsg.2013.10.008

Duffaud, F., Brun, L., Planchut, B., 1966. Le bassin du Sud-Ouest marocain. In: Reyre, D. (Ed.), Bassins sédimentaires du littoral africain, 1ère partie. Association des Services Géologiques Africains, Paris, pp. 5–12.

El Mhamdi, A., Habib, A., Tajdi, A., et al., 2024. Accuracy assessment and enhancement of global DEMs for drainage morphometric analysis: a case study from Aïn Leuh Region, Morocco. Model. Earth Syst. Environ., 10, 3375–3409. https://doi.org/10.1007/s40808-024-01961-0

Ettachfini, E.M., Fekkak, A., Ouanaimi, H., Jouhari, A., Ezzouhairi, H., Ettachfini, M., Hilali, M., Michard, A., 2018. Carte Géologique du Maroc au 1/50 000, Feuille Azegour – Notice explicative. Notes et Mém. Serv. Géol. Maroc, 589 bis, 111 pp.

Fekkak, A., Ettachfini, E.M., Ouanaimi, H., Toufiq, A., Ezzouhairi, H., Jouhari, A., Company, M., Andreu, B., El Attari, A., Michard, A., 2018. Notice explicative de la carte géologique du Maroc au 1/50 000, feuille Addouz, 590 bis. Notes et Mém. Serv. Géol. Maroc, 115.

Frizon De Lamotte, Z., M., Missenard, Y., Hafid, M., El Azzouzi, M., Maury, R., Charriere, A., Taki, Z., Benammi, M., Michard, A., 2008. The Atlas System. In: Michard, A., Saddiqi, O., Chalouan, A., Frizon De Lamotte, D. (Eds.), Continental Evolution: The Geology of Morocco. Springer, pp. 133–202.

Froitzheim, N., 1984. Oberkretazische Vertikallektionik im Hohen Atlas SW von Marrakech, Marokko – Rekonstruktion eines Bewegungsablaufs im Frühstadium der Atlas-Orogenese. N. Jb. Geol. Paläont. Mh., 8, 463–471.

Habib, A., Berrada, I., Najih, A., Lagnaoui, A., Fadili, A., El Adnani, A., Arrad, T.Y., Laaziz, A.Y., in press. Analysis of co-seismic deformation using SAR interferometry: insights into the 2023 Al Haouz earthquake, Morocco. In: Proc. Mediterranean Geosciences Union (MedGU) 2024, Advances in Science, Technology & Innovation (ASTI) series, Springer.

Habib, A., Berrada, I., El Adnani, A., Laaziz, Y.A., Fadili, A., Lagnaoui, A., Najih, A., Arrad, T.Y., 2025. DInSAR Analysis of Ground Deformation Induced by the 2023 Al Haouz Earthquake, Morocco. Int. Arch. Photogramm. Remote Sens. Spatial Inf. Sci., XLVIII-M-6-2025, 127–131. https://doi.org/10.5194/isprs-archives-XLVIII-M-6-2025-127-2025

Habib, A., Labbassi, K., Delgado Blasco, J.M., van Leijen, F., Iannini, L., Menenti, M., 2017. Land deformation monitoring using PS-InSAR technique over Sahel-Doukkala (Morocco). Proc. Int. Conf. Adv. Technol. Signal Image Process. (ATSIP), Fez, Morocco, pp. 1–6. https://doi.org/10.1109/ATSIP.2017.8075576

Hamdi, L., Defaflia, N., Merghadi, A., Fehdi, C., Yunus, A.P., Dou, J., Pham, Q.B., Abdo, H.G., Almohamad, H., Al-Mutiry, M., 2023. Ground Surface Deformation Analysis Integrating InSAR and GPS Data in the Karstic Terrain of Cheria Basin, Algeria. Remote Sens., 15, 1486. https://doi.org/10.3390/rs15061486

Hawker, L., Uhe, P., Paulo, L., Sosa, J., Savage, J., Sampson, C., Neal, J., 2022. A 30 m global map of elevation with forests and buildings removed. Environ. Res. Lett. https://doi.org/10.1088/1748-9326/ac4d4f

Hughes, P.D., Fenton, C.R., Gibbard, L., 2011. Quaternary Glaciations of the Atlas Mountains, North Africa. In: Ehlers, J., Gibbard, P.L., Hughes, P.D. (Eds.), Developments in Quaternary Science, Vol. 15. Amsterdam, The Netherlands, pp. 1065–1074.

Ibrahim, H.B., Salah, M., Zarzoura, F.H.F., et al., 2025. Mapping of surface deformation associated with the 7.8 magnitude Turkey earthquake of 6 Feb 2023 using radar interferometry. Innov. Infrastruct. Solut., 10, 49. https://doi.org/10.1007/s41062-024-01856-0

Li, Q., Wang, W., Wang, J., Zhang, J., Geng, D., 2021. Exploring the relationship between InSAR coseismic deformation and earthquake-damaged buildings. Remote Sens. Environ., 262, 112508. https://doi.org/10.1016/j.rse.2021.112508

Luo, Z., Zhou, L., Qin, J., Wen, X., Zhang, D., Li, X., Qin, D., 2024. Assessing surface deformation in the Chengdu Plain: A comprehensive time-series InSAR study of urban development and natural environmental factors. Adv. Space Res., 73(3), 1780–1798. https://doi.org/10.1016/j.asr.2023.11.043

Michard, A., Soulaimani, A., Hoepffner, C., Ouanaimi, H., Baidder, L., Rjimati, E., Saddiqi, O., 2010. The Southwestern branch of the Variscan Belt: evidence from Morocco. Tectonophysics, 492, 1–24.

Ramzan, U., Fan, H., Aeman, H., Ali, M., Al-Qaness, M.A., 2022. Combined analysis of PS-InSAR and hypsometry integral (HI) for comparing seismic vulnerability and assessment of various regions of Pakistan. Sci. Rep., 12, 22423. https://doi.org/10.1038/s41598-022-26159-1

Torre, D., Galve, J.P., Reyes-Carmona, C., et al., 2024. Geomorphological assessment as basic complement of InSAR analysis for landslide processes understanding. Landslides, 21, 1273–1292. https://doi.org/10.1007/s10346-024-02216-w

Wahid Abbas, S., Ali, S., Reicherter, K., 2022. Seismicity and landform development of the dextral Kalabagh Fault Zone, Pakistan: Implications from morphotectonics and paleoseismology. Tectonophysics, 822, 229182. https://doi.org/10.1016/j.tecto.2021.229182